

Spin-wave dispersion measurement by variable-gap propagating spin-wave spectroscopy

Marek Vaňatka,^{1,*} Krzysztof Szulc,² Ondřej Wojewoda,¹ Carsten Dubs,³ Andrii Chumak,⁴ Maciej Krawczyk,² Oleksandr V. Dobrovolskiy,⁴ Jarosław W. Klos,² and Michal Urbánek^{1,5,†}

¹*CEITEC BUT, Brno University of Technology, 612 00 Brno, Czech Republic*

²*ISQI, Faculty of Physics, Adam Mickiewicz University, Poznań, Poland*

³*INNOVENT e.V. Technologieentwicklung, 07745 Jena, Germany*

⁴*Faculty of Physics, University of Vienna, A-1090 Wien, Austria*

⁵*Institute of Physical Engineering, Brno University of Technology, 616 69 Brno, Czech Republic*

(Dated: July 21, 2021)

Magnonics is seen nowadays as a candidate technology for energy-efficient data processing in classical and quantum systems. Pronounced nonlinearity, anisotropy of dispersion relations and phase degree of freedom of spin waves require advanced methodology for probing spin waves at room as well as at mK temperatures. Yet, the use of the established optical techniques like Brillouin light scattering (BLS) or magneto optical Kerr effect (MOKE) at ultra-low temperatures is forbiddingly complicated. By contrast, microwave spectroscopy can be used at all temperatures but is usually lacking spatial and wavenumber resolution. Here, we develop a variable-gap propagating spin-wave spectroscopy (VG-PSWS) method for the deduction of the dispersion relation of spin waves in wide frequency and wavenumber range. The method is based on the phase-resolved analysis of the spin-wave transmission between two antennas with variable spacing, in conjunction with theoretical data treatment. We validate the method for the in-plane magnetized CoFeB and YIG thin films in $\mathbf{k} \perp \mathbf{B}$ and $\mathbf{k} \parallel \mathbf{B}$ geometries by deducing the full set of material and spin-wave parameters, including spin-wave dispersion, hybridization of the fundamental mode with the higher-order perpendicular standing spin-wave modes and surface spin pinning. The compatibility of microwaves with low temperatures makes this approach attractive for cryogenic magnonics at the nanoscale.

I. INTRODUCTION

Properties of magnetic materials are of high interest due to several application concepts regarding, e.g., memories, sensors, microwave devices, or logic devices [1]. In the emerging field of magnonics, which utilizes spin-waves for data transport and processing, the essential system characteristic is the spin-wave dispersion relation. It provides a connection between the k -space and frequency space, and it also dictates other properties like the group velocity v_g and decay length Λ . In thin films (approx. below 30 nm), only the fundamental mode is observed when the experimentally accessible frequency range is limited to few GHz. In contrast, the spin-wave dispersion of thicker films can be rather complex as multiple perpendicularly standing modes may appear in the spectrum, exhibiting frequency crossing and hybridization [2]. The spin-wave dispersion measurement is typically done by k -resolved [2, 3] or phase-resolved [4, 5] Brillouin Light Scattering (BLS). Current interest in quantum computing, quantum magnonics [6] and in superconductor/ferromagnet hybrid systems [7, 8], rises the need for material characterization at ultra-low temperatures, where optical access is typically extremely complicated. All electrical measurements are usually preferable in these applications.

The spin-wave dispersion measurement is also possible using the propagating spin-wave spectroscopy (PSWS). The PSWS is a technique which uses a vector network analyzer (VNA) connected to a pair of microwave antennas (e.g., striplines or coplanar waveguides) by microwave probes [9, 10]. The two antennas (i.e., spin-wave transmitter and receiver) have a gap between them over which the spin-waves propagate, as shown in Fig. 1(a). Transmitting antenna is powered by the VNA's microwave source and the receiving antenna serves as an induction pick-up detected by the VNA's second port. The antenna type determines the excitation properties and can be adjusted to the experiment. Main three types of antennas used in experiments are striplines (rectangular wires), U-shaped ground-signal (GS) antennas, and coplanar waveguide (CPW) antennas. Schematic geometry of all three antenna types is shown in Fig. 1 (b). Striplines provide a continuous spectrum where the maximum excited k -vector is limited by the stripline width. Ciubotaru et al. [11] showed scalability of the antennas, where 125 nm wide striplines provided a wide continuous k -vector band. Good alternatives are GS antennas, e.g. [9, 12, 13], or coplanar waveguides (CPW), e.g. [14–17], both providing a filtering capability for the k -vector spectrum allowing only specific ranges to exist. PSWS can be used on both nanostructured materials (stripes) [11–15, 18, 19] as well as layers [17, 20]. It was previously shown that the PSWS signal can be negligibly different for continuous layers and wide stripes [17]. PSWS signals can also be modeled [15, 17, 21].

In previous reports, the spin-wave dispersion was ex-

* marek.vanatka@live.com

† michal.urbanek@ceitec.vutbr.cz

tracted from PSWS spectra measured on yttrium iron garnet (YIG) using the CPW excitation. As the CPWs excitation spectrum exhibits distinct peaks in k -space, it allows extracting one point in spin-wave dispersion for each peak. The central k -vector of each peak is then assigned to a frequency from either the envelope of the S_{21} sweep [18, 22] or by fitting the S_{21} spectrum [17]. This approach is limited to only several extracted points, and it is not easily transferable to metallic materials because of the low signal amplitude (compared to YIG) caused by large damping, making it impossible to use more than two peaks from the CPW antenna's excitation spectrum.

Here, we show that the spin-wave dispersion measurement using VNA is possible with a high level of details determined by the VNA frequency step.

II. MEASUREMENT SETUP AND SAMPLE PREPARATION

Our setup uses Rohde & Schwarz ZVA50 VNA and GGB industries microwave probes to establish a connection to the two antennas lithographically fabricated on top of CoFeB and YIG thin films. The lithography process consisted of e-beam patterning using PMMA resist, e-beam evaporation of Ti 5 nm/Cu 85 nm/Au 10 nm multilayer, and lift-off. The CoFeB films (nominal thicknesses 30 nm and 100 nm) were magnetron-sputtered from $\text{Co}_{40}\text{Fe}_{40}\text{B}_{20}$ (at. %) target on (100) GaAs substrate with 5 nm Ta buffer layer. The (111) YIG films were grown by liquid phase epitaxy on top of a 500 μm , thick (111) gadolinium gallium garnet substrate [23, 24]. The samples were placed in a gap of a rotatable electromagnet allowing to apply an in-plane magnetic field up to 400 mT in an arbitrary direction with respect to the spin-wave propagation direction. The VNA was set using a calibration substrate supplied with the microwave probes. A power sweep was performed before measuring each type of the sample-antenna combination to find a suitable power level that avoids nonlinear phenomena [25] and maintains a sufficient signal-to-noise ratio.

The VNA controls and analyses the electric signals of transmitting and receiving antennas both in the domain of amplitude and phase, therefore, it can measure the phase acquired by the spectral components of spin wave while it propagates between antennas. Our analysis is based on the S_{21} transmission parameter. The transmitted spin-wave signal is modified by a nonmagnetic background $S_{21}^{\text{background}}$ that is always present in the experiment due to direct electromagnetic crosstalk between the antennas. This background is constant for different values of static magnetic field, and therefore it is possible to evaluate it as the median over all measured magnetic fields. The subtracted signal ΔS_{21} is then calculated as: $\Delta S_{21} = S_{21} - S_{21}^{\text{background}}$.

Fig. 1 (c,d) shows the ΔS_{21} signal, measured at 0 dBm power output for a 30 nm CoFeB thin film, over the gap 1.8 μm in the $\mathbf{k} \perp \mathbf{B}$ geometry (magnetostatic surface

waves), and with 500 nm wide striplines used as excitation and detection antennas. This geometry is known to be nonreciprocal with an exponential distribution of the dynamic magnetization along the layer's thickness due to the surface localization of the mode [26, 27]. The higher signal amplitude in the $+B$ part of the spectrum is caused by both the stronger excitation and by the larger induction pick up from spin-waves propagating at the nearer surface. To achieve the best result, we can focus on $+B$ part of the spectrum (or alternatively on the $-B$ part and use the reverse transmission parameter S_{21}). Fig.

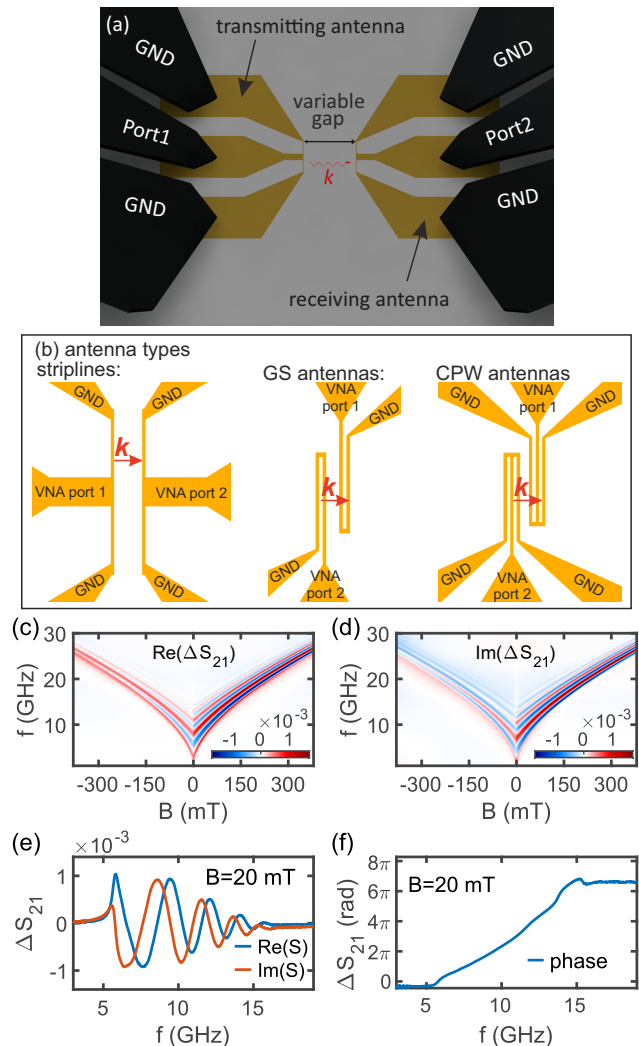


FIG. 1. (a) Schematics of the PSWS experiment using a pair of stripline antennas. (b) Schematic geometry of the three most commonly used antenna types. The outcomes of the PSWS measurement: (c) real and (d) imaginary part of $\Delta S_{21}(B, f)$ for 30 nm thick CoFeB layer 30 nm in $\mathbf{k} \perp \mathbf{B}$ geometry and the gap width of 1.8 μm . The measurement shows the nonreciprocity of spin-wave propagation for the $\mathbf{k} \perp \mathbf{B}$ geometry which is reflected by the larger signal in $+B$ fields than in $-B$ fields. The plots of (e) show real and imaginary parts of $\Delta S_{21}(f)$, and (f) the unwrapped phase of $\Delta S_{21}(f)$, at fixed field $B = 20$ mT.

1(d) shows the plot of real and imaginary parts of ΔS_{21} measured at 20 mT. The corresponding phase, which was unwrapped, is shown in Fig. 1(e). The phase rises from the ferromagnetic resonance (FMR) frequency up until it reaches the antenna's excitation limits. Beyond this point, the signal loses its coherency due to insufficient signal-to-noise ratio, and therefore the phase stops evolving. The slope of the phase depends on the gap size – it changes more rapidly for wider gaps.

In the next step, we repeat the measurement on multiple instances of identical antenna structures (with varying gap width) prepared on the same 30 nm CoFeB thin film sample. The phases measured over 11 gap widths are shown in Fig. 2(a). The phases are on the same level before the frequency reaches FMR, and then they start to rise. The lowest phase corresponds to the smallest gap width and the uppermost to the largest measured gap width. Then we project the measured phases into a phase – gap width plot [selected frequencies are plotted in Fig. 2(b)]. In this projection, the phase shows a linear dependence (for a coherent plane wave) that can be fitted; the slope equals to the k -vector at the given frequency. Now we can plot the extracted k -vectors against their frequencies, showing the resulting dispersion relation in Fig. 2(c). To confirm the result, we remeasured the same sample using phase-resolved BLS, and we found a very good agreement. The comparison of the dispersion relations measured by both techniques (VNA – red, BLS – blue) is shown in Fig. 2(c), and the comparison of the measured phase evolution at the frequency of 11.5 GHz is shown in Fig. 2(d).

III. MEASURED SPIN-WAVE DISPERSION RELATIONS

Fig. 3(a) shows dispersion relations of the same 30 nm CoFeB thin film measured in $\mathbf{k} \perp \mathbf{B}$ geometry in magnetic fields ranging from 20 mT to 380 mT with a step of 60 mT. The sample was also measured in $\mathbf{k} \parallel \mathbf{B}$ geometry, but the measured signal was insufficient to reconstruct the dispersion relation. For all measured fields, it was possible to evaluate the dispersion for k -vectors ranging from 0 up to 8 rad/ μm . The upper limit is given by the excitation efficiency [15] of the used antenna (see blue lines in Fig. 3). By fitting the measured dispersions using the Kalinikos-Slavin model [28], we were able to obtain material parameters of the measured thin films (see black lines in Fig. 3 for the model fits and the figure caption for the fitting results).

In addition to the 30 nm CoFeB thin film, we also measured 100 nm thick CoFeB [Fig. 3(b)] and 100 nm thick YIG [Fig. 3(c)] films to further explore the possibilities of the presented technique. The measurements were performed using different antenna types (stripline, GS, CPW) to see their influence on the quality of the obtained dispersions, and they were also evaluated for multiple magnetic fields in $\mathbf{k} \perp \mathbf{B}$ and in $\mathbf{k} \parallel \mathbf{B}$ geometries. The

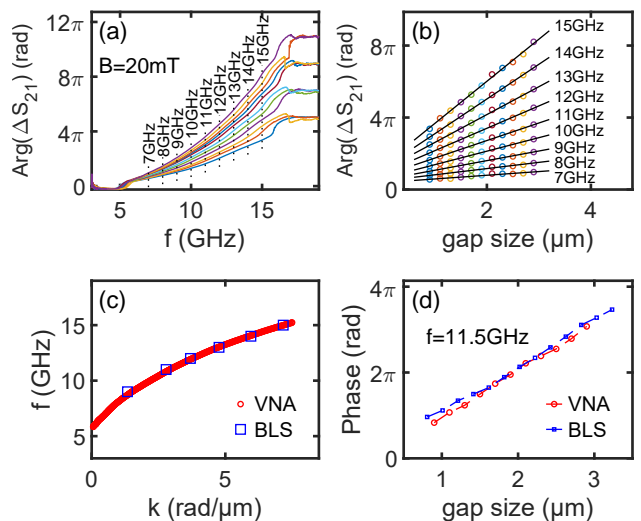


FIG. 2. Extraction of the dispersion relation from the outcomes of PSWS experiment on 30 nm CoFeB thin film at $B = 20$ mT in $\mathbf{k} \perp \mathbf{B}$ geometry. (a) The unwrapped ΔS_{21} phases measured over gap widths ranging from 0.9 μm (the lowest line) to 2.9 μm (the steepest line) with the step of 200 nm. (b) The representative fits of the phase at selected frequencies versus gap size where the slope of the fit yields the desired k -vector at that frequency. (c) The dispersion relation extracted for all frequencies within the range with sufficient PSWS signal (red line). The dispersion obtained by phase-resolved BLS is plotted in the blue points for comparison. (d) The compared outcomes of the phase measurements for VNA (red circles) and phase-resolved BLS (blue squares) at single frequency $f = 11.5$ GHz.

100 nm thick CoFeB film was measured in the fields ranging from 20 to 380 mT with a step of 60 mT at a power of 0 dBm. In Fig. 3(b) we show the dispersion measured using 500 nm wide stripline antenna for $\mathbf{k} \perp \mathbf{B}$ geometry and with 500 nm coplanar waveguide (signal and ground line widths, as well as signal-to-ground gap, were 500 nm) in $\mathbf{k} \perp \mathbf{B}$ geometry. We were able to obtain a dispersion in $\mathbf{k} \parallel \mathbf{B}$ geometry also using a 500 nm wide stripline antenna but with substantially worse quality due to its lower excitation efficiency. The 100 nm thick YIG film was measured in $\mathbf{k} \perp \mathbf{B}$ and $\mathbf{k} \parallel \mathbf{B}$ geometries in the fields ranging from 20 to 200 mT with a step of 20 mT at a power of -30 dBm. In this case, it was possible to obtain a dispersion in both geometries using all types of antennas. Fig. 3(c) shows data acquired by GS antennas with gap widths from 1.0 to 3.4 μm with 400 nm step. As in the case of the coplanar waveguide, the dimensions of the GS antennas were 500 nm (signal and ground line widths and signal-to-ground gap width). The dispersions are plotted for magnetic fields from 20 to 200 mT with a step of 20 mT and the power output was set to -30 dBm.

In the dispersion measured on 100 nm thick CoFeB film, we further identified visible hybridizations at the crossings' positions between the $n = 0$ fundamental spin-wave mode and $n = 1, 2, 3$ higher-order perpendicularly

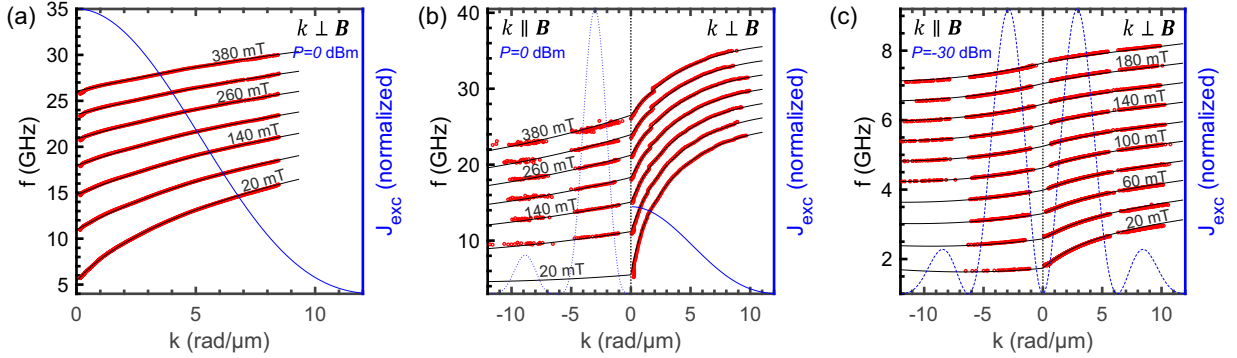


FIG. 3. The dispersion relations measured using the PSWS technique (red points) compared to the analytic dispersions from Kalinikos-Slavin model (black lines) for (a) 30 nm thick CoFeB (b) 100 nm thick CoFeB, (c) 100 nm thick YIG layers. For clarity, the data for $\mathbf{k} \perp \mathbf{B}$ are plotted in the domain of positive wave numbers k and the $\mathbf{k} \parallel \mathbf{B}$ data are presented with negative k . The samples were excited by stripline, CPW, and GS antennas with all lateral wire widths dimensions of 500 nm. The blue lines show calculated (and normalized) wave number excitation spectra of the antennas, calculated from the spatial distributions of microwave field (the solid, dashed and dotted lines correspond to the spectra of stripline, GS, and CPW antenna, respectively). For Kalinikos-Slavin model we fitted the following values of parameters: (a) $M_s = 1230$ kA/m ($\mu_0 M_s = 1.54$ T), $\gamma/2\pi = 30.5$ GHz/T, $t = 29.0$ nm; (b) $M_s = 1310$ kA/m ($\mu_0 M_s = 1.64$ T), $\gamma/2\pi = 30.1$ GHz/T; (c) $M_s = 133$ kA/m ($\mu_0 M_s = 0.166$ T), $\gamma/2\pi = 28.3$ GHz/T, where t stands for thickness of the layer. In fitting procedure, we fixed the exchange stiffness to $A_{\text{ex}} = 15$ pJ/m³ for CoFeB films and $A_{\text{ex}} = 3.6$ pJ/m³ for the YIG film.

standing spin-wave modes (see Fig. 4). The hybridizations are present in the measured dispersion relation as gap openings, with a portion of the measured data evolving towards smaller k -vectors [see Fig. 4(d) for the most prominent example]. This part of the dispersion has no physical meaning and is only a result of the data processing described earlier in the text. The hybridizations are also directly visible as dips in the magnitude $\text{Abs}(\Delta S_{21})$ of the transmission spectra [see Fig. 4(b)].

IV. NUMERICAL MODELING

To investigate numerically the hybridization between the fundamental mode and perpendicularly standing modes, we solve Landau-Lifshitz equation (LLE) using the finite-element method (FEM) in the frequency domain. The LLE was linearized and implemented in FEM solver (COMSOL Multiphysics) as a set of differential equations for in-plane and the out-of-plane components of magnetization m_{\parallel} and m_{\perp} :

$$i\omega m_{\parallel} = |\gamma|\mu_0 \left[(H_0 - \frac{2A_{\text{ex}}}{\mu_0 M_s} \Delta) m_{\perp} + M_s \partial_{x_{\perp}} \varphi \right], \quad (1)$$

$$i\omega m_{\perp} = |\gamma|\mu_0 \left[(H_0 - \frac{2A_{\text{ex}}}{\mu_0 M_s} \Delta) m_{\parallel} + M_s \partial_{x_{\parallel}} \varphi \right], \quad (2)$$

together with the equation for the scalar magnetostatic potential φ derived from Maxwell equations in magnetostatic approximation [29, 30]:

$$\Delta \varphi - \partial_{x_{\parallel}} m_{\parallel} - \partial_{x_{\perp}} m_{\perp} = 0, \quad (3)$$

where x_{\parallel} and x_{\perp} denote the directions of the corresponding dynamic components of magnetization.

In contrast to the analytical model of Kalinikos and Slavin, our numerical calculations truly reproduce the spin dispersion relation in the crossover dipolar-exchange regime [2], including the hybridizations between the fundamental spin-wave mode and perpendicularly standing spin-wave modes. In our model, we also consider the presence of surface anisotropy K_s . The anisotropy is expected to be different on the bottom and the top faces of the magnetic layer interfaced with different materials. The surface anisotropy and its asymmetry (between the top and bottom face) is responsible for the spin-wave pinning and the strength of the hybridization between fundamental and perpendicularly standing modes. The pinning is implemented in the boundary conditions [31]

$$\partial_{x_{\perp}} m_{\parallel} = 0, \quad (4)$$

$$A_{\text{ex}} \partial_{x_{\perp}} m_{\perp} - K_s m_{\perp} = 0. \quad (5)$$

The numerical model (as well as the analytical model by Kalinikos and Slavin) is characterized by a few material parameters. We fixed the value of exchange stiffness to $A_{\text{ex}} = 14$ pJ/m² and layer's thickness to nominal value $d = 100$ nm. The values of saturation magnetization $M_s = 1275$ kA/m and gyromagnetic ratio $|\gamma|/2\pi = 30.8$ GHz/T were selected to fit the ferromagnetic resonance frequency (i.e., the frequency of fundamental mode at $k = 0$) and the slope of the dispersion for fundamental mode. The surface anisotropy K_s determines the spin-wave pinning and therefore is important both for the quantization (and the frequencies) of the perpendicularly standing modes and the strength of the hybridization between and perpendicularly standing modes. To obtain the proper values of the frequencies

of perpendicularly standing modes, we did not need to reduce the thickness below the nominal value 100 nm but we had to introduce the non-zero K_s instead, which seems to be a more realistic approach. The experimental data show that the hybridizations of fundamental mode with the perpendicularly standing modes are observed both for the perpendicularly standing modes quantized with even ($n = 2$) and odd number of nodes ($n = 1, 3$) across the layer. The effect for $n = 1, 3$ is hardly visible in dispersion relation [Fig. 4(c,e)] but is quite distinctive in the measurement of the transmission amplitude [Fig. 4(b)]. These results indicate that the asymmetric pinning (and different values of surface anisotropy on both faces of the CoFeB layer) must be considered to obtain less symmetric profiles of spin-wave modes across the thickness of the layer, which in turn, gives the non-zero cross-sections between fundamental mode and perpendicularly standing modes of odd numbers of nodes. There is always some degree of freedom for choosing the values of K_s on both faces, therefore, we decided to consider the simplest case where $K_s = 0$ and $1600 \mu\text{J}/\text{m}^2$ at the top (interface with vacuum) and bottom (interface with GaAs). With these values, we succeeded in the induction of the hybridization of fundamental mode ($n = 0$) with the first ($n = 1$) and third ($n = 3$) perpendicularly standing modes, characterized by the width comparable to the widths of the deeps of the transmission ΔS_{21} [orange stripes in Fig. 4(a,b)]. It is worth noting that in the case of symmetric pinning (we took $K_s = 700 \mu\text{J}/\text{m}^2$ on both faces), we do not observe the hybridization with the first ($n = 1$) and third ($n = 3$) perpendicularly standing modes [see blue dashed lines in Fig. 4(c,e)].

V. ADDITIONAL DATA ANALYSIS AND DISCUSSION

From the measured dispersion relations, it is possible to extract also other parameters important for spin-wave propagation. The group velocity v_g can be calculated as the numerical derivative of the dispersion $v_g = 2\pi df/dk$ and the lifetime τ can be obtained as the numerical derivative of field-dependent dispersion [29]: $\tau = (\alpha\omega \frac{\partial\omega}{\partial\omega_B})^{-1} = (\frac{\alpha 4\pi^2 f}{\gamma} \frac{\partial f}{\partial B})^{-1}$, where $\omega_B = \gamma B$ and α is a damping constant.

The decay length δ can be then calculated by multiplying the group velocity and the lifetime $\delta = v_g\tau$. In Fig. 5(a), we plot the decay length obtained by the above-described procedure (orange line) and compare it with the decay length obtained using the more traditional approach, i.e., by fitting the exponential decay of the magnitude of ΔS_{21} signal (blue line). Here, the decay length δ was obtained by fitting [see Fig. 5(b) for representative fits] the formula $\text{Abs}(\Delta S_{21}) = Ie^{-g/\delta}$ in logarithmic form $\ln[\text{Abs}(\Delta S_{21})] = \ln(I) - \frac{1}{\delta}g$, where g is the gap distance, and I is a free parameter proportional to signal strength. In Fig. 5(c), we plot field-dependent lifetime evaluated using the decay length obtained from the

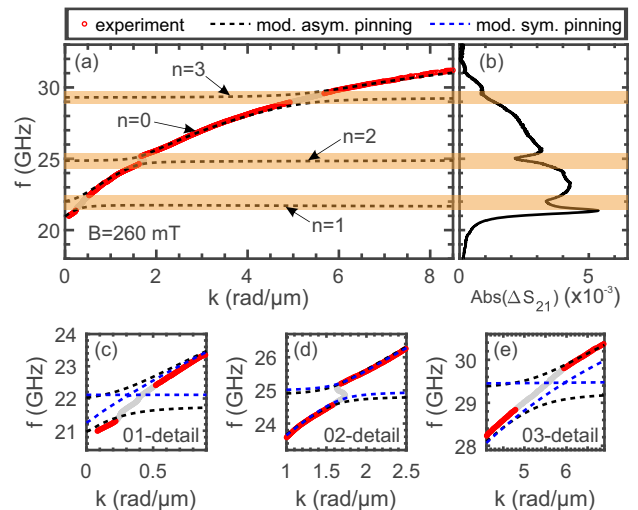


FIG. 4. (a) Measured dispersion relation (red points) for 100 nm thick CoFeB layer at 260 mT exhibiting hybridized spin-wave modes, visible mainly at the $n = 02$ crossing. The dashed line represents dispersion simulation with asymmetrical surface pinning conditions with parameters $K_s = 0$ and $1600 \mu\text{J}/\text{m}^2$ on top and bottom face of the layer, respectively. (b) Corresponding magnitude of the ΔS_{21} transmission parameter exhibiting dips at the crossings' positions ($|\text{Abs}(\Delta S_{21})|$ data shown for the gap width of $1.8 \mu\text{m}$). (c-e) Details of the 01, 02, and 03 crossings, respectively. Dashed blue lines correspond to the case of symmetric pinning ($K_s = 700 \mu\text{J}/\text{m}^2$ on both faces).

derivative of field-dependent dispersion ($\partial\omega/\partial\omega_B$, orange circles) and from fitting the exponential decay of the magnitude of ΔS_{21} signal (blue diamonds). Both approaches give roughly the same results for both the decay length and the lifetime, but the decay lengths obtained using the $\partial\omega/\partial\omega_B$ approach agree better with the analytical model [see Fig. 5(a), green line]. The lower quality of the data obtained from fitting the exponential decay of the magnitude of ΔS_{21} signal is caused by the limitation of our experimental arrangement. Due to the finite length of the excitation antenna, spin-wave caustics can form [32]. An example of such caustics measured by BLS microscopy is shown in Fig. 5(e). The phase in the caustic beam is spatially incoherent [33] and the focusing effect [34] causes modulation of the spin-wave intensity along the propagation direction. The associated adverse effects can be avoided by measuring at propagation distances that are sufficiently small with respect to the stripline length. In our experiments, we used the stripline length of $10 \mu\text{m}$, and the maximum measured propagation distance was $2.9 \mu\text{m}$. For phase-resolved measurement such as evaluation of dispersions, the short propagation distance was sufficient. On the other hand, the change in signal at $2.9 \mu\text{m}$ propagation distance was not sufficient to obtain a fully reliable fit of the exponential decay of the ΔS_{21} magnitude and at longer propagation distances the measurements were distorted by caustics.

We also analyzed how the number of measured propa-

gation distances (gaps) affected the reliability of the obtained dispersion. We took the data measured for 11 gap widths in total and then used different combinations of a reduced number of gap widths (starting from 2 up to 10) to evaluate the dispersion. The dispersion obtained from the reduced number of gap widths was then compared to the analytical fit Kalinikos-Slavin model [28] of the dispersion obtained from fitting of the complete set of 11 measured points. As shown in Fig. 5(d), the mean frequency difference from the reference dispersion can rise to the maximum of 400 MHz when using a combination of just two gap widths. This maximum quickly decreases to 200 MHz for five gap widths and then stays around 100 MHz for combinations of six and more gaps.

As can be seen from the presented data, the variable-gap approach allows the reconstruction of the spin-wave dispersion relation, including detailed features that might be used for analysis of the spin-wave system. In order to obtain the highest possible data quality, we need to fabricate multiple pairs of antennas where the gap width and the step in the gap width (an increase of the gap between two pairs of antennas) must be optimized for each experiment. Note that this approach does not require precise knowledge of the excitation spot location (phase origin) because it does not affect the fit's slope. It is only essential to know the relative differences between the propagation distances, i.e., the gap-width step, which can be easily measured (and precisely fabricated using e-beam lithography).

The antenna design is sample-specific and needs to be tailored to fulfil experimental requirements. The antenna's type and geometry must be able to excite the expected k -vector range with sufficient efficiency.

The gap widths need to be in the optimum range considering the caustics formation and the spin-wave decay length for the given material and geometry. For example, for CoFeB 30 nm in $k \parallel \mathbf{B}$ geometry at $k = 5 \text{ rad}/\mu\text{m}$, we calculated decay lengths of $0.03 \mu\text{m}$ and $0.45 \mu\text{m}$ for magnetic fields of 20 and 200 mT, respectively. Here, the quality of the measured data, even for the smallest fabricated gap distance of $1 \mu\text{m}$, was not sufficient to evaluate dispersion; thus, this geometry is not presented in Fig. 3(a).

Before fitting the data as plotted in Fig. 2(b), the phase needs to be correctly unwrapped. In the case of stripline antennas with a continuous excitation spectrum, it is possible to achieve correct unwrap even when the phases for neighboring gap widths at the same frequency are higher than π rad by unwrapping the phase in the frequency spectrum [Fig. 2(a)]. It is because the frequency step size of the VNA is usually small and the phase shift of the neighboring points is always smaller than π rad. On the other hand, the safest approach is to unwrap the phases when plotted against the gap size [Fig. 2(b)]. In this case, the phase change of neighboring points must be smaller than π rad. This is necessary for antenna types with discrete excitation spectra (i.e., CPW, GS, ladders [42] or meanders [43]).

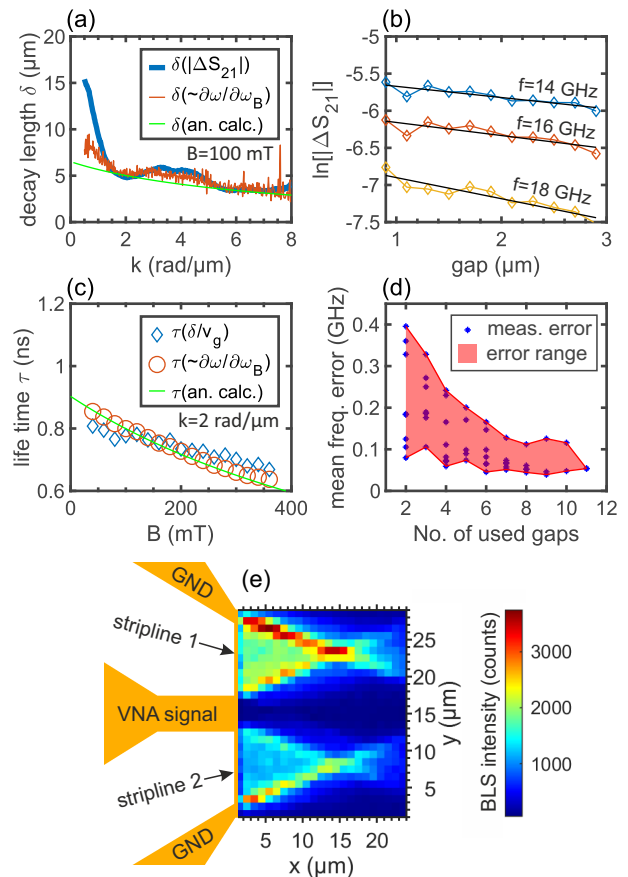


FIG. 5. The determination of decay length and lifetime from VG-PSWS measurement of 30 nm thick CoFeB film (a-c,e) and the impact of the number of gaps on the quality of the result (d). (a) Blue line shows the spin-wave decay lengths obtained directly from exponential fits, orange line shows the decay length calculated by multiplication of the life time and the group velocity and the green line is calculated from the Kalinikos-Slavin model. (b) Representative exponential fits of the ΔS_{21} magnitude which were used to obtain the spin-wave propagation length. (c) Spin-wave life time extracted from the derivative of field-dependent dispersion using $\alpha = 0.075$ (orange circles), calculated by dividing the propagation length (from ΔS_{21} magnitude) by the numerically calculated group velocity (blue diamonds) and calculated from the Kalinikos-Slavin model (green line). (d) Mean frequency difference of the dispersion obtained from the reduced number of gap widths compared to the analytical fit of the dispersion obtained from the complete set of 11 measured points. Blue points represent different combinations of gaps and the red area represents the difference spread. (e) Spin-wave caustics caused by the finite length of the antenna, measured on 100 nm CoFeB film by BLS with excitation frequency of 11 GHz in the external magnetic field of 26 mT. Caustics can destroy the phase coherence of propagating spin-waves. Note that all presented data were collected at propagation distances (gap widths) between $0.9 \mu\text{m}$ to $2.9 \mu\text{m}$ to avoid the negative effects of the caustics formation.

TABLE I. Comparison of experimental techniques used for measurement of spin-wave dispersion relations.

	Lateral resolution in (nm)	Resolution in k (rad/ μm)	Resolution in f (Hz)	Phase extraction	max k (rad/ μm)	Experimental geometries (MS, BV, FV)
VG-PSWS [this work]	-	$< 0.1^*$	1	yes	10^{***}	MS, BV, (FV possible)
PSWS [17, 21]	-	2^{***}	1	no	10^{***}	MS, BV, FV
MOKE [35, 36]	500	$< 0.1^*$	$1 \cdot 10^8^{**}$	yes	10	BV, MS
Conventional BLS [2, 37]	10,000	0.5	$1 \cdot 10^8$	no	23.6	BV, MS
Phase-resolved BLS [4, 38, 39]	250	$< 0.1^*$	$1 \cdot 10^8^{**}$	yes	7	BV, MS
STXM [40, 41]	20	$< 0.1^*$	$1 \cdot 10^8^{**}$	yes	30	BV, MS

MS - magnetostatic surface spin waves, BV - backward volume spin waves, FV - forward volume spin waves

* The k -resolution can be tailored to the magnetic system under study by an appropriate design of the experiment geometry.

**The resolution in f in these techniques is limited by the acquisition time.

*** Excitation limited.

The step in the gap width defines the maximum k -vector for which the dispersion can be measured. The phase change of the spin wave along the step distance has to be smaller than π rad except for certain cases discussed later. On the other hand, small k -vectors may have a phase change that is too small over a short step in the gap width. If we require an accurate fitting of small k -vectors, the step in the gap width should be large enough to provide sufficient phase change (we suggest at least 1 rad) while respecting the decay length.

VI. METHOD COMPARISON

In Table 1, we compare the variable gap propagating spin-wave spectroscopy with other experimental techniques used to obtain spin-wave dispersion relations. To get detailed dispersion, one needs to have high resolution in both the k -vector and the frequency. Optical and X-ray techniques have low frequency resolution, which is typically limited to hundreds of MHz. In the case of conventional BLS, the resolution is determined directly by the Fabry-Perot interferometer [44]. The optical techniques using microwave excitation, i.e., Magneto-Optical Kerr Effect microscopy (MOKE), Phase-resolved BLS and Scanning Transmission X-ray Microscopy (STXM), are limited by slow signal acquisition. It does not allow capturing the required span of frequencies with a high resolution in a reasonable time. The propagating spin-wave spectroscopy technique, which uses known positions of the excitation peaks of the CPW antenna, can capture the data with a high resolution in frequency. However, the k -resolution is limited with the finite widths of peaks in the excitation spectra of the used CPW antennas which in turn affect also the frequency resolution.

Big advantage of the VG-PSWS technique is that it does not require direct optical access to the sample, making the method very suitable for, e.g., experiments at ultra-low temperatures. In addition, compared to other techniques for spin-wave dispersion relation measurement VG-PSWS can achieve high resolution in frequency and

k -vector at the same time. This combination allows capturing smooth dispersion curves over the span of all accessible k -vectors and fast acquisition times allow repeating the experiment in multiple magnetic field strengths and orientations. The full set of field-dependent dispersion curves measured for both $\mathbf{k} \perp \mathbf{B}$ and in $\mathbf{k} \parallel \mathbf{B}$ geometries present a robust 4-dimensional (f , k , B , angle) dataset that can be further evaluated, and all essential material and spin-wave parameters can be extracted from it.

A disadvantage of this method is the need for a set of antennas with multiple gap widths on top of the sample. The other techniques can obtain the dispersion either without any antenna (conventional BLS), with one excitation antenna (MOKE, Phase-resolved BLS, STXM) or with a pair of excitation and detection antennas (PSWS). However, the need for multiple antennas may be overcome in the future by using freestanding positionable antennas [45].

VII. CONCLUSION

In conclusion, we presented a new method of extraction of high-quality spin-wave dispersion relation from propagating spin-wave spectroscopy (PSWS) measurements performed over several propagation distances. We demonstrated this technique on CoFeB and YIG thin films measured in $\mathbf{k} \perp \mathbf{B}$ and $\mathbf{k} \parallel \mathbf{B}$ geometries. The results on CoFeB thin film were verified by phase-resolved BLS measurement showing good agreement. When compared with the phase-resolved BLS, the VNA-based method provides more frequency measurement points in a shorter acquisition time. Fine detail measurement capability was demonstrated on the measurement and analysis of hybridized modes acquired on 100 nm thick CoFeB thin film, revealing asymmetric surface pinning and the values of pinning parameters on both interfaces of the magnetic layer. The all electric nature of this method makes it very suitable for characterization of cryogenic and quantum magnonics systems and materials.

ACKNOWLEDGMENTS

The work was supported by MEYS CR (project CZ.02.2.69/0.0/0.0/19_073/0016948). CzechNanoLab project LM2018110 is gratefully acknowledged for the financial support of the measurements and sample fabrication at CEITEC Nano Research Infrastructure. O.W. was supported by Brno PhD talent

scholarship. J.W.K. and M.K. acknowledge the support of the National Science Centre - Poland for the projects UMO-2020/37/B/ST3/03936 and UMO-2020/39/O/ST5/02110. O.V.D. acknowledges the Austrian Science Fund (FWF) for support through Grant No. I 4889 (CurviMag). C.D. gratefully acknowledges financial support from the Deutsche Forschungsgemeinschaft (DFG, German Research Foundation) - 271741898.

-
- [1] B. Dieny, I. L. Prejbeanu, K. Garello, P. Gambardella, P. Freitas, R. Lehnendorff, W. Raberg, U. Ebels, S. O. Demokritov, J. Akerman, A. Deac, P. Pirro, C. Adelman, A. Anane, A. V. Chumak, A. Hirohata, S. Mangin, S. O. Valenzuela, M. C. Onbaşlı, M. d'Aquino, G. Prenat, G. Finocchio, L. Lopez-Diaz, R. Chantrell, O. Chubykalo-Fesenko, and P. Bortolotti, Opportunities and challenges for spintronics in the microelectronics industry, *Nature Electronics* **3**, 446 (2020).
- [2] S. Tacchi, R. Silvani, G. Carlotti, M. Marangolo, M. Edrrief, A. Rettori, and M. G. Pini, Strongly hybridized dipole-exchange spin waves in thin Fe-N ferromagnetic films, *Physical Review B* **100**, 104406 (2019).
- [3] C. Mathieu, J. Jorzick, A. Frank, S. O. Demokritov, A. N. Slavin, B. Hillebrands, B. Bartenlian, C. Chappert, D. Decanini, F. Rousseaux, and E. Cambril, Lateral Quantization of Spin Waves in Micron Size Magnetic Wires, *Physical Review Letters* **81**, 3968 (1998).
- [4] K. Vogt, H. Schultheiss, S. J. Hermsdoerfer, P. Pirro, A. A. Serga, and B. Hillebrands, All-optical detection of phase fronts of propagating spin waves in a Ni81Fe19 microstripe, *Applied Physics Letters* **95**, 182508 (2009).
- [5] V. E. Demidov, S. Urazhdin, and S. O. Demokritov, Control of spin-wave phase and wavelength by electric current on the microscopic scale, *Applied Physics Letters* **95**, 262509 (2009).
- [6] D. Lachance-Quirion, S. P. Wolski, Y. Tabuchi, S. Kono, K. Usami, and Y. Nakamura, Entanglement-based single-shot detection of a single magnon with a superconducting qubit, *Science* **367**, 425 (2020).
- [7] O. V. Dobrovolskiy, R. Sachser, T. Brächer, T. Böttcher, V. V. Kruglyak, R. V. Vovk, V. A. Shklovskij, M. Huth, B. Hillebrands, and A. V. Chumak, Magnon-fluxon interaction in a ferromagnet/superconductor heterostructure, *Nature Physics* **15**, 477 (2019).
- [8] I. A. Golovchanskiy, N. N. Abramov, V. S. Stolyarov, V. V. Bolginov, V. V. Ryazanov, A. A. Golubov, and A. V. Ustinov, Ferromagnet/Superconductor Hybridization for Magnonic Applications, *Advanced Functional Materials* **28**, 1802375 (2018).
- [9] M. Bailleul, D. Olligs, C. Fermon, and S. O. Demokritov, Spin waves propagation and confinement in conducting films at the micrometer scale, *Europhysics Letters (EPL)* **56**, 741 (2001).
- [10] T. Devolder, G. Talmelli, S. M. Ngom, F. Ciubotaru, C. Adelman, and C. Chappert, Measuring the dispersion relations of spin wave bands using time-of-flight spectroscopy, *Physical Review B* **103**, 214431 (2021).
- [11] F. Ciubotaru, T. Devolder, M. Manfrini, C. Adelman, and I. P. Radu, All electrical propagating spin wave spectroscopy with broadband wavevector capability, *Applied Physics Letters* **109**, 012403 (2016).
- [12] K. Yamanoi, S. Yakata, T. Kimura, and T. Manago, Spin Wave Excitation and Propagation Properties in a Permalloy Film, *Japanese Journal of Applied Physics* **52**, 083001 (2013).
- [13] U. K. Bhaskar, G. Talmelli, F. Ciubotaru, C. Adelman, and T. Devolder, Backward volume vs Damon-Eshbach: A traveling spin wave spectroscopy comparison, *Journal of Applied Physics* **127**, 033902 (2020).
- [14] M. Bailleul, D. Olligs, and C. Fermon, Propagating spin wave spectroscopy in a permalloy film: A quantitative analysis, *Applied Physics Letters* **83**, 972 (2003).
- [15] V. Vlaminck and M. Bailleul, Spin-wave transduction at the submicrometer scale: Experiment and modeling, *Physical Review B* **81**, 014425 (2010).
- [16] P. Gruszecki, M. Kasprzak, A. E. Serebryannikov, M. Krawczyk, and W. Śmigaj, Microwave excitation of spin wave beams in thin ferromagnetic films, *Scientific Reports* **6**, 22367 (2016).
- [17] H. Qin, S. J. Hämäläinen, K. Arjas, J. Witteveen, and S. van Dijken, Propagating spin waves in nanometer-thick yttrium iron garnet films: Dependence on wave vector, magnetic field strength, and angle, *Physical Review B* **98**, 224422 (2018).
- [18] H. Yu, O. d'Allivy Kelly, V. Cros, R. Bernard, P. Bortolotti, A. Anane, F. Brandl, R. Huber, I. Stasinopoulos, and D. Grundler, Magnetic thin-film insulator with ultra-low spin wave damping for coherent nanomagnonics, *Scientific Reports* **4**, 6848 (2015).
- [19] M. Collet, O. Gladii, M. Evelt, V. Bessonov, L. Soumah, P. Bortolotti, S. O. Demokritov, Y. Henry, V. Cros, M. Bailleul, V. E. Demidov, and A. Anane, Spin-wave propagation in ultra-thin YIG based waveguides, *Applied Physics Letters* **110**, 092408 (2017).
- [20] A. Krysztofik, H. Głowiński, P. Kuświk, S. Zietek, L. E. Coy, J. N. Rychły, S. Jurga, T. W. Stobiecki, and J. Dubowik, Characterization of spin wave propagation in (1 1 1) YIG thin films with large anisotropy, *Journal of Physics D: Applied Physics* **50**, 235004 (2017).
- [21] M. Sushruth, M. Grassi, K. Ait-Oukaci, D. Stoeffler, Y. Henry, D. Lacour, M. Hehn, U. Bhaskar, M. Bailleul, T. Devolder, and J.-P. Adam, Electrical spectroscopy of forward volume spin waves in perpendicularly magnetized materials, *Physical Review Research* **2**, 043203 (2020).
- [22] J. Chen, F. Heimbach, T. Liu, H. Yu, C. Liu, H. Chang, T. Stückler, J. Hu, L. Zeng, Y. Zhang, Z. Liao, D. Yu, W. Zhao, and M. Wu, Spin wave propagation in perpendicularly magnetized nm-thick yttrium iron garnet films, *Journal of Magnetism and Magnetic Materials* **450**, 3

- (2018).
- [23] C. Dubs, O. Surzhenko, R. Linke, A. Danilewsky, U. Brückner, and J. Dellith, Sub-micrometer yttrium iron garnet LPE films with low ferromagnetic resonance losses, *Journal of Physics D: Applied Physics* **50**, 204005 (2017).
- [24] C. Dubs, O. Surzhenko, R. Thomas, J. Osten, T. Schneider, K. Lenz, J. Grenzer, R. Hübner, and E. Wendler, Low damping and microstructural perfection of sub-40nm-thin yttrium iron garnet films grown by liquid phase epitaxy, *Physical Review Materials* **4**, 024416 (2020).
- [25] K. Zakeri, J. Lindner, I. Barsukov, R. Meckenstock, M. Farle, U. von Hörsten, H. Wende, W. Keune, J. Rucker, S. S. Kalarickal, K. Lenz, W. Kuch, K. Baberschke, and Z. Frait, Spin dynamics in ferromagnets: Gilbert damping and two-magnon scattering, *Physical Review B* **76**, 104416 (2007).
- [26] T. Schneider, A. A. Serga, T. Neumann, B. Hillebrands, and M. P. Kostylev, Phase reciprocity of spin-wave excitation by a microstrip antenna, *Physical Review B* **77**, 214411 (2008).
- [27] K. Sekiguchi, K. Yamada, S. M. Seo, K. J. Lee, D. Chiba, K. Kobayashi, and T. Ono, Nonreciprocal emission of spin-wave packet in FeNi film, *Applied Physics Letters* **97**, 022508 (2010).
- [28] B. A. Kalinikos and A. N. Slavin, Theory of dipole-exchange spin wave spectrum for ferromagnetic films with mixed exchange boundary conditions, *Journal of Physics C: Solid State Physics* **19**, 7013 (1986).
- [29] D. D. Stancil and A. Prabhakar, *Spin Waves* (Springer US, Boston, MA, 2009).
- [30] J. Rychlý and J. W. Klos, Spin wave surface states in 1D planar magnonic crystals, *Journal of Physics D: Applied Physics* **50**, 164004 (2017).
- [31] G. Rado and J. Weertman, Spin-wave resonance in a ferromagnetic metal, *Journal of Physics and Chemistry of Solids* **11**, 315 (1959).
- [32] T. Schneider, A. A. Serga, A. V. Chumak, C. W. Sandweg, S. Trudel, S. Wolff, M. P. Kostylev, V. S. Tiberkevich, A. N. Slavin, and B. Hillebrands, Non-diffractive Subwavelength Wave Beams in a Medium with Externally Controlled Anisotropy, *Physical Review Letters* **104**, 197203 (2010).
- [33] H. S. Körner, J. Stigloher, and C. H. Back, Excitation and tailoring of diffractive spin-wave beams in NiFe using nonuniform microwave antennas, *Physical Review B* **96**, 100401 (2017).
- [34] V. Veerakumar and R. E. Camley, Magnon focusing in thin ferromagnetic films, *Physical Review B* **74**, 214401 (2006).
- [35] R. Dreyer, N. Liebing, E. R. J. Edwards, A. Müller, and G. Woltersdorf, Spin-wave localization and guiding by magnon band structure engineering in yttrium iron garnet, *Physical Review Materials* **5**, 064411 (2021).
- [36] H. Qin, R. B. Holländer, L. Flajšman, F. Hermann, R. Dreyer, G. Woltersdorf, and S. van Dijken, Nanoscale magnonic Fabry-Pérot resonator for low-loss spin-wave manipulation, *Nature Communications* **12**, 2293 (2021).
- [37] T. Sebastian, K. Schultheiss, B. Obry, B. Hillebrands, and H. Schultheiss, Micro-focused Brillouin light scattering: imaging spin waves at the nanoscale, *Frontiers in Physics* **3**, 10.3389/fphy.2015.00035 (2015).
- [38] L. Flajšman, K. Wagner, M. Vaňatka, J. Gloss, V. Křižáková, M. Schmid, H. Schultheiss, and M. Urbánek, Zero-field propagation of spin waves in waveguides prepared by focused ion beam direct writing, *Physical Review B* **101**, 014436 (2020).
- [39] O. Wojewoda, T. Hula, L. Flajšman, M. Vaňatka, J. Gloss, J. Holobrádek, M. Staňo, S. Stienen, L. Körber, K. Schultheiss, M. Schmid, H. Schultheiss, and M. Urbánek, Propagation of spin waves through a Néel domain wall, *Applied Physics Letters* **117**, 022405 (2020).
- [40] F. Groß, N. Träger, J. Förster, M. Weigand, G. Schütz, and J. Gräfe, Nanoscale detection of spin wave deflection angles in permalloy, *Applied Physics Letters* **114**, 012406 (2019).
- [41] J. Förster, S. Wintz, J. Bailey, S. Finizio, E. Josten, C. Dubs, D. A. Bozhko, H. Stoll, G. Dieterle, N. Träger, J. Raabe, A. N. Slavin, M. Weigand, J. Gräfe, and G. Schütz, Nanoscale X-ray imaging of spin dynamics in yttrium iron garnet, *Journal of Applied Physics* **126**, 173909 (2019).
- [42] W. Bang, M. B. Jungfleisch, J. Lim, J. Trossman, C. C. Tsai, A. Hoffmann, and J. B. Ketterson, Excitation of the three principal spin waves in yttrium iron garnet using a wavelength-specific multi-element antenna, *AIP Advances* **8**, 056015 (2018).
- [43] J. Lucassen, C. F. Schippers, L. Rutten, R. A. Duine, H. J. M. Swagten, B. Koopmans, and R. Lavrijsen, Optimizing propagating spin wave spectroscopy, *Applied Physics Letters* **115**, 012403 (2019).
- [44] F. Scarponi, S. Mattana, S. Corezzi, S. Caponi, L. Comez, P. Sassi, A. Morresi, M. Paolantoni, L. Urbanelli, C. Emiliani, L. Roscini, L. Corte, G. Cardinali, F. Palombo, J. Sandercock, and D. Fioretto, High-Performance Versatile Setup for Simultaneous Brillouin-Raman Microspectroscopy, *Physical Review X* **7**, 031015 (2017).
- [45] T. Hache, M. Vaňatka, L. Flajšman, T. Weinhold, T. Hula, O. Ciubotariu, M. Albrecht, B. Arkook, I. Barsukov, L. Fallarino, O. Hellwig, J. Fassbender, M. Urbánek, and H. Schultheiss, Freestanding Positionable Microwave-Antenna Device for Magneto-Optical Spectroscopy Experiments, *Physical Review Applied* **13**, 054009 (2020).